

# Characterization of kaolinized nontronite by visible to near infrared (VNIR) reflectance spectroscopy: implication for the genesis of compositional stratigraphy on Mars

Xiaorong Qin<sup>1</sup>, Jiacheng Liu<sup>2</sup>, Wei Tan<sup>3</sup>, Hongping He<sup>3</sup>, Joseph Michalski<sup>2</sup>, Yu Sun<sup>4</sup>, Shangying Li<sup>5</sup>, Binlong Ye<sup>2</sup>, and Yi-Liang Li<sup>2</sup>

<sup>1</sup>Guangzhou Institute of Geochemistry, Chinese Academy of Sciences, Guangzhou, China

<sup>2</sup>University of Hong Kong

<sup>3</sup>Guangzhou Institute of Geochemistry, Chinese Academy of Sciences

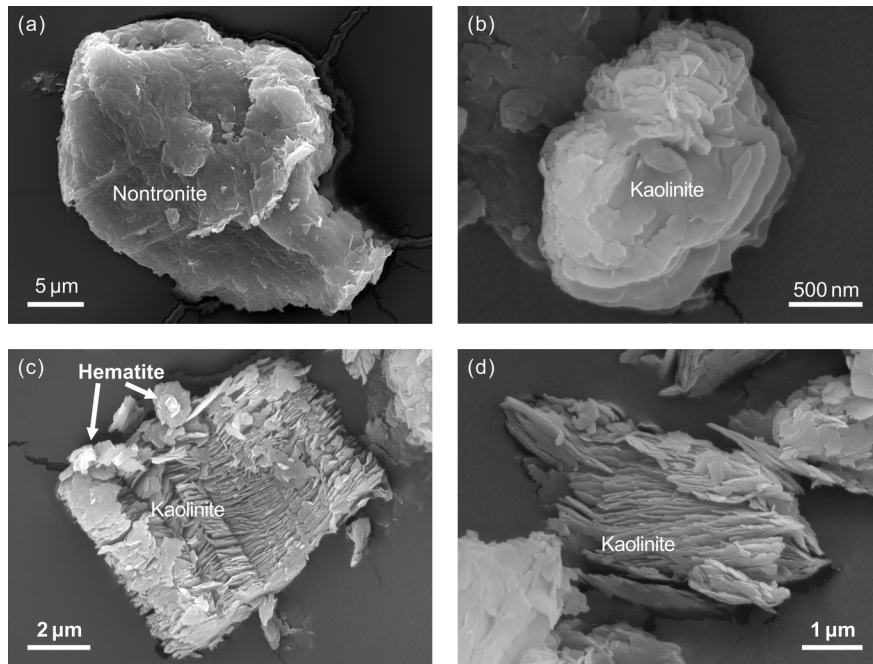
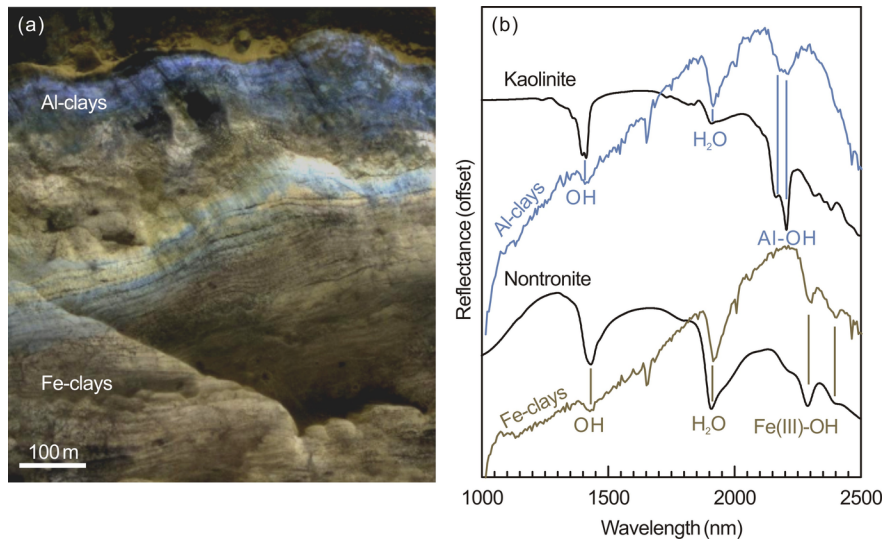
<sup>4</sup>Institute of Geology and Geophysics, Chinese Academy of Sciences

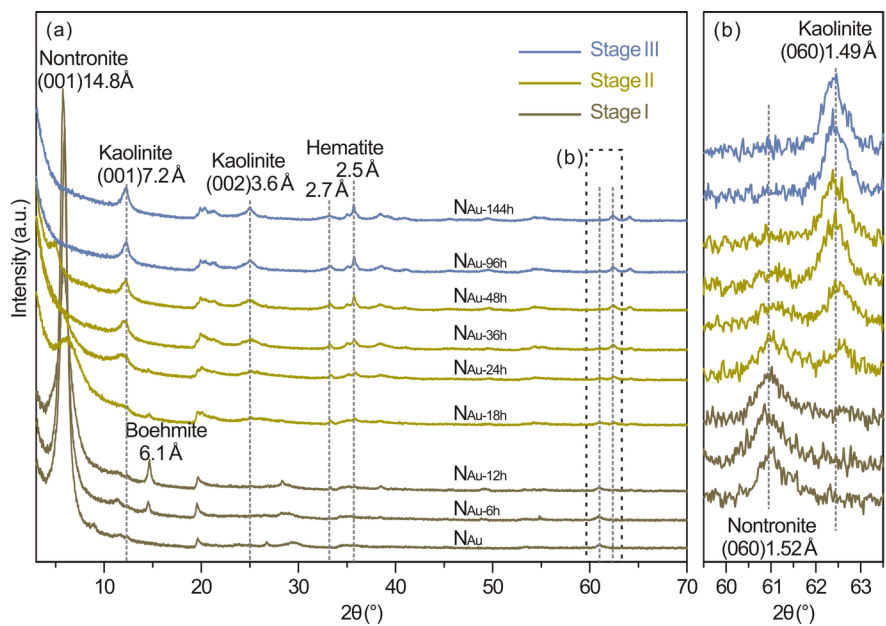
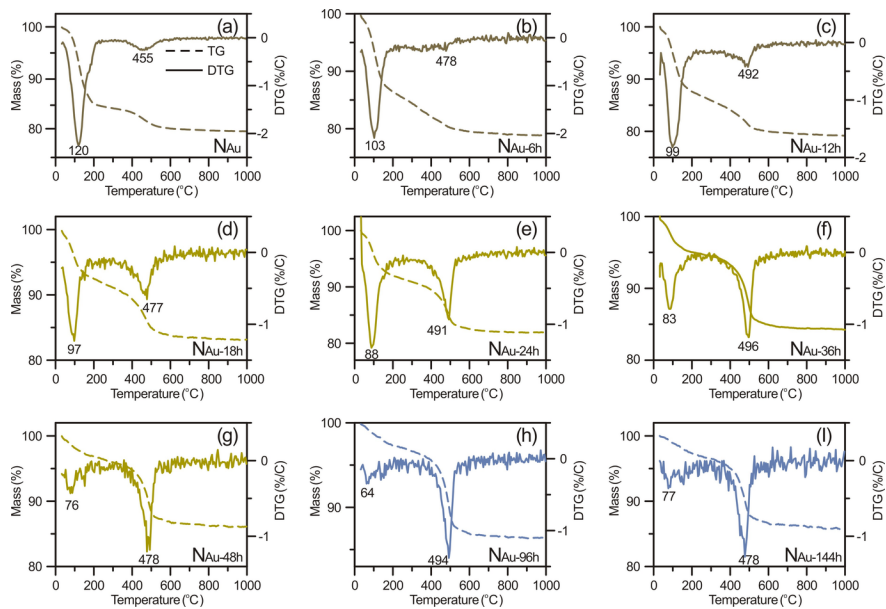
<sup>5</sup>Chang'an University

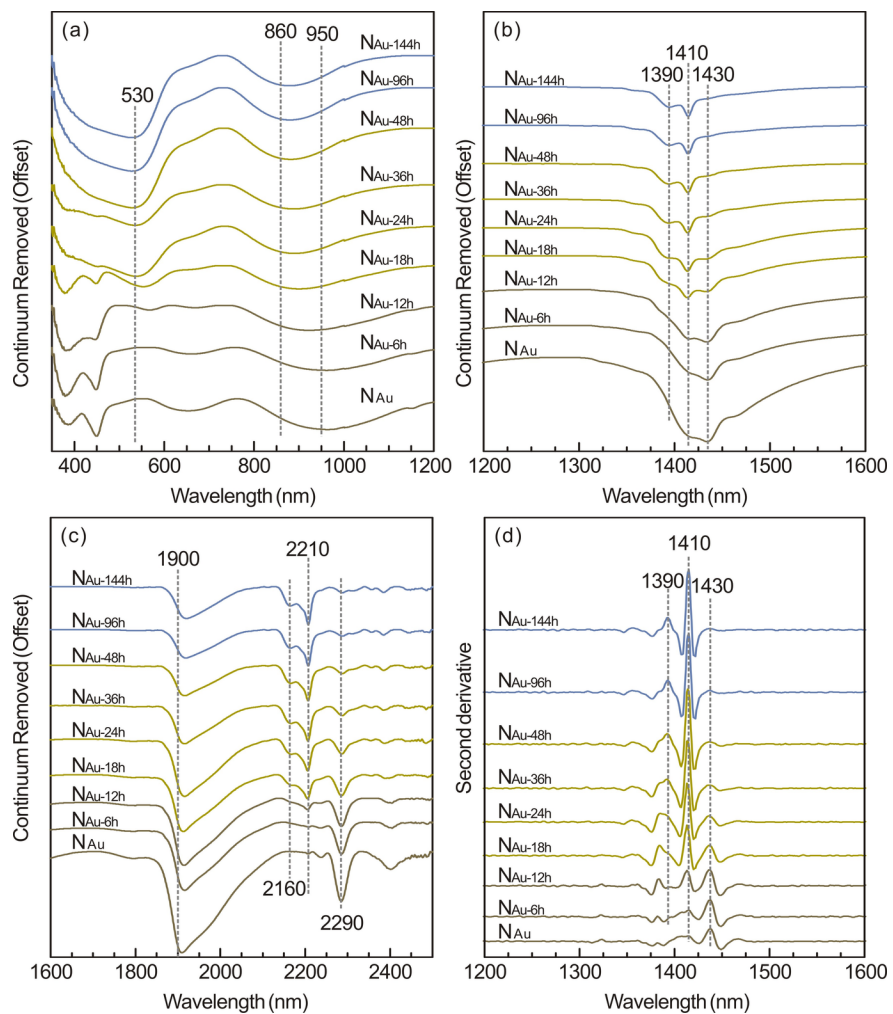
December 7, 2022

## Abstract

Compositional stratigraphy, consisting of Al-rich kaolinite overlying Fe/Mg-rich nontronite, is sporadically distributed within 40°S to 30°N on Mars. The compositional stratigraphy was considered a typical product of a warm and wet climate, and a window into understanding the atmospheric conditions of early Mars. However, the question remains as to whether the compositional stratigraphy was formed by chemical weathering or sedimentation. Variations in mineralogical/geochemical properties along the compositional stratigraphy can provide important clues for interpreting the genesis of the compositional stratigraphy. Visible to near infrared (VNIR) reflectance spectroscopy has been used as an effective tool to quantitatively characterize the abundance of kaolinite, nontronite, and weathering intensity in a basaltic weathering succession, as demonstrated by a terrestrial regolith profile. Nevertheless, the VNIR spectra could be influenced by primary minerals and organics in a basalt succession. To test the effectiveness of spectral parameters, the stepwise transformation of nontronite to kaolinite was experimentally modeled and quantitatively investigated using thermogravimetric (TG) and VNIR. The correlation between BD1400 and the content of OH, BD1900 and the H<sub>2</sub>O content, and BD1400/BD1900 and the OH/H<sub>2</sub>O ratio were quantitatively constrained to demonstrate their effectiveness as spectral proxies. The obtained data set was also compared with the VNIR spectra from the compositional stratigraphy on Mars, and the continuous variations of the spectral proxies suggest the compositional stratigraphy is formed by a surface chemical weathering process. Accordingly, Mars likely had a warm and wet climate that could maintain liquid water on its surface over a geologic time span.







1       **Characterization of kaolinized nontronite by visible to near infrared (VNIR)**  
2                   **reflectance spectroscopy: implication for the genesis of compositional**  
3                                   **stratigraphy on Mars**

4   Xiaorong Qin<sup>1,2,3</sup>, Jiacheng Liu<sup>4</sup>, Wei Tan<sup>1,2\*</sup>, Hongping He<sup>1,2,3</sup>, Joseph Michalski<sup>4</sup>, Yu  
5                                   Sun<sup>5</sup>, Shangying Li<sup>6</sup>, Binlong Ye<sup>4</sup>, Yiliang Li<sup>4</sup>

6   1 CAS Key Laboratory of Mineralogy and Metallogeny/Guangdong Provincial Key  
7   Laboratory of Mineral Physics and Materials, Guangzhou Institute of Geochemistry,  
8   Chinese Academy of Sciences, Guangzhou, China

9   2 CAS Center for Excellence in Deep Earth Science, Guangzhou, China

10  3 University of Chinese Academy of Sciences, Beijing, China

11  4 Laboratory for Space Research, University of Hong Kong, Hong Kong, China

12  5 Key Laboratory of Earth and Planetary Physics, Institute of Geology and Geophysics,  
13  Chinese Academy of Sciences (CAS), Beijing, China

14  6 School of Land Engineering, Chang'an University, Xi'an, China

15  \* Corresponding author: Wei Tan ([tanwei@gig.ac.cn](mailto:tanwei@gig.ac.cn))

16

17  **Key points:**

- 18  ● VNIR reflectance spectroscopy is effective in assessing the OH and H<sub>2</sub>O content  
19    in different stages of kaolinized nontronite.
- 20  ● The VNIR data set is reliable for identifying kaolinite/ nontronite ratios and  
21    weathering intensities in a basaltic weathering succession.
- 22  ● The continuous variation of BD1400/BD1900 ratios suggest the compositional  
23    stratigraphy on Mars was formed by a chemical weathering process.

24

25 **Abstract**

26 Compositional stratigraphy, consisting of Al-rich kaolinite overlying Fe/Mg-  
27 rich nontronite, is sporadically distributed within 40 °S to 30 °N on Mars. The  
28 compositional stratigraphy was considered a typical product of a warm and wet climate,  
29 and a window into understanding the atmospheric conditions of early Mars. However,  
30 the question remains as to whether the compositional stratigraphy was formed by  
31 chemical weathering or sedimentation. Variations in mineralogical/ geochemical  
32 properties along the compositional stratigraphy can provide important clues for  
33 interpreting the genesis of the compositional stratigraphy. Visible to near infrared  
34 (VNIR) reflectance spectroscopy has been used as an effective tool to quantitatively  
35 characterize the abundance of kaolinite, nontronite, and weathering intensity in a  
36 basaltic weathering succession, as demonstrated by a terrestrial regolith profile.  
37 Nevertheless, the VNIR spectra could be influenced by primary minerals and organics  
38 in a basalt succession. To test the effectiveness of spectral parameters, the stepwise  
39 transformation of nontronite to kaolinite was experimentally modeled and  
40 quantitatively investigated using thermogravimetric (TG) and VNIR. The correlation  
41 between BD1400 and the content of OH, BD1900 and the H<sub>2</sub>O content, and  
42 BD1400/BD1900 and the OH/H<sub>2</sub>O ratio were quantitatively constrained to demonstrate  
43 their effectiveness as spectral proxies. The obtained data set was also compared with  
44 the VNIR spectra from the compositional stratigraphy on Mars, and the continuous  
45 variations of the spectral proxies suggest the compositional stratigraphy is formed by a

46 surface chemical weathering process. Accordingly, Mars likely had a warm and wet  
47 climate that could maintain liquid water on its surface over a geologic time span.

48

#### 49 **Plain Language Summary**

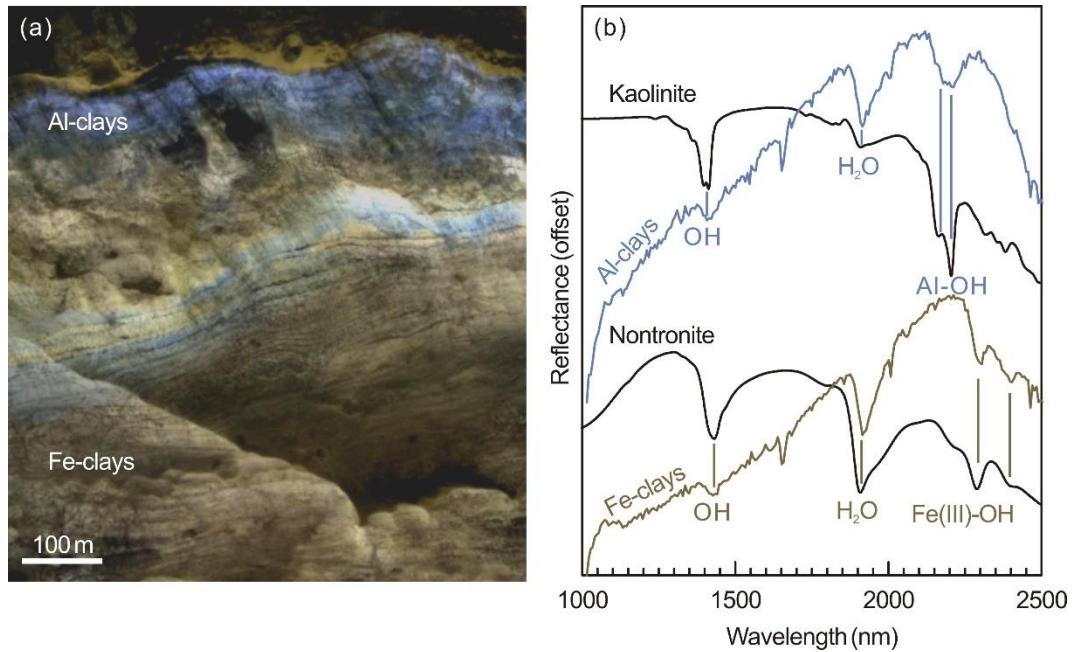
50       Compositional stratigraphy consisting of kaolinite overlying nontronite is an  
51 intriguing landscape on the surface of Mars. However, it is still unclear how the  
52 compositional stratigraphy is formed. An analogous study suggests that it may have  
53 been formed by top-down chemical weathering as is the case with a terrestrial regolith  
54 profile, since the features of spectral proxies BD1400/BD1900 in the compositional  
55 stratigraphy become progressively stronger from bottom to top. Nevertheless, the  
56 aforementioned spectral proxies could potentially be influenced by variations in  
57 protolithic minerals and/or organics in the basaltic succession. To test the effectiveness  
58 of spectral parameters on weathering intensity in a basaltic succession and to discuss  
59 the genesis of compositional stratigraphy, the stepwise transformation of nontronite to  
60 kaolinite was experimentally modeled and quantitatively investigated using TG and  
61 VNIR. Accordingly, the gradual upward increasing trend of VNIR spectra ratios  
62 BD1400/BD1900 in the compositional stratigraphy on the Mars reflect gradual  
63 decomposition of nontronite, formation of kaolinite and increasing weathering intensity.  
64 Therefore, the compositional stratigraphy on the Mars is likely formed by a surface  
65 chemical weathering process and Mars likely experienced a warm and wet climate  
66 capable of sustaining liquid water on its surface over a geologic time span.

67

## 68 **1 Introduction**

69 Clay minerals have been discovered at numerous sites on the Martian surface,  
70 including the Nili Fossae region, north of the Syrtis Major volcanic plateau, in the  
71 Mawrth Vallis region, and Gale Crater (Bibring et al., 2006; Bristow et al., 2021; Carter  
72 et al., 2013; Ehlmann et al., 2011a, 2011b; Viviano et al., 2013). One of the most  
73 exciting discoveries is the compositional stratigraphy ubiquitous in the Eridania Basin,  
74 Noachis Terra, Nili Fossae, Valles Marineris and Mawrth Vallis (Figure 1a), located  
75 within 40°S to 30°N (Bishop et al., 2018; Carter et al., 2015; Gaudin et al., 2011;  
76 Michalski et al., 2010, 2013; Wray et al., 2008, 2009). Most of the compositional  
77 stratigraphy on the Mars developed from the Late Noachian to the Early Hesperian, and  
78 is characterized by Al-rich kaolinite and underlying Fe/Mg nontronite (Figure 1b)  
79 (Carter et al., 2015; Gaudin et al., 2011; Liu et al., 2021b; Michalski et al., 2013).

80 The compositional stratigraphy was considered to be detrital phyllosilicate  
81 sediments deposited in lacustrine, alluvial, and aeolian environments due to their  
82 layered appearance and served as lithologic evidence for the presence of lakes on the  
83 ancient terrains of Mars (Bishop et al., 2020; Lowe et al., 2020; McKeown et al., 2009;  
84 Michalski et al., 2010; Michalski & Noe Dobrea, 2007). Nevertheless, the genesis of  
85 compositional stratigraphy has also been attributed to top-down chemical weathering  
86 of the Fe/Mg-clay bearing crust or to basaltic deposition under different climatic  
87 conditions, as the contact between the different Al-rich and Fe/Mg-rich clay units is  
88 conformable (Bishop et al., 2018; Carter et al., 2015; Ehlmann et al., 2013; Gainey et  
89 al., 2014; Gaudin et al., 2011; Liu et al., 2021b; Ye & Michalski, 2021).



90  
 91 **Figure 1.** Mineral distribution and infrared spectroscopy of a compositional stratigraphy profile in  
 92 the Mawrth Vallis region, Mars. (a) View of typically compositional stratigraphy, *i.e.*, Al-clays (blue  
 93 tone) overlying Fe-clays (brown tone), in a Muara crater wall at Mawrth Vallis region (HiRISE  
 94 image, PSP\_004052\_2045, located at 340.68° E, 24.35° N, data from Planetary Data System); (b)  
 95 Comparison between CRISM spectra of Al-clays (blue) and Fe-clays (brown) and reference  
 96 spectra of nontronite and kaolinite. Note that the spectrum of Fe clays is identical to nontronite, and  
 97 the spectrum of Al-clays is identical to kaolinite. The reference spectra of kaolinite and nontronite  
 98 were collected from the Maoming Kaolin Clay Company in Guangdong Province, China, and the  
 99 Uley Graphite Mine in South Australia, respectively.

100

101 A proper constraint on the genesis of compositional stratigraphy is a necessary  
 102 prerequisite for considering it as a window to understanding the past climate and  
 103 atmospheric conditions of the early Mars (Gaudin et al., 2011; Liu et al., 2021b).  
 104 Visible/near infrared (VNIR) reflectance spectra provide by far the most reliable and  
 105 effective data set for identifying chemical and mineralogical features of stratigraphy on  
 106 the Mars (Chauviré et al., 2021; Cuadros et al., 2016; Fox et al., 2021; Michalski et al.,  
 107 2015; Pineau et al., 2022; Viviano-Beck et al., 2014). The absorption bands at ~1400,  
 108 ~1900, ~2200 and ~2290 nm are essentially related to OH (octahedral metal-OH, metal

109 = Al, Fe and Mg) and H<sub>2</sub>O (interlayer water) of kaolinite and nontronite (Bibring et al.,  
110 2005; Ehlmann et al., 2013; Pineau et al., 2022). Accordingly, remote sensing VNIR  
111 spectra show that the compositional stratigraphy is characterized by Al-rich kaolinite  
112 and underlying Fe/Mg-rich nontronite (Figure. 1b) (Carter et al., 2015; Ehlmann et al.,  
113 2013; Gaudin et al., 2011; Liu et al., 2021b; Michalski et al., 2013).

114 Analogous to the compositional stratigraphy on the Mars, some terrestrial basalt  
115 weathering successions evolve from nontronite of 2:1 type to kaolinite of 1:1 type due  
116 to progressive chemical weathering (Gaudin et al., 2011; Liu et al., 2021a; Prudencio  
117 et al., 2002). During the chemical weathering, hydrolysis leads to the formation of OH  
118 by the reaction of water with Al and/ or Fe in the octahedral sheet of kaolinite, and  
119 leaching tends to reduce both alkaline (earth) elements and H<sub>2</sub>O (interlayer water)  
120 within the interlayer of nontronite (Cuadros & Michalski, 2013; Liu et al., 2021a).  
121 Therefore, the changes in the content of OH and H<sub>2</sub>O during the transformation of  
122 nontronite to kaolinite are essentially related to the weathering intensity of a basaltic  
123 weathering succession (Liu et al., 2021a). It was suggested that the VNIR spectral  
124 proxies for variations of OH and H<sub>2</sub>O, *e.g.*, BD1400/BD1900, were positively  
125 correlated with the weathering intensity of terrestrial weathering successions (Liu et al.,  
126 2021a;). The early study also suggested that the compositional stratigraphy in Mawrth  
127 Vallis was likely formed by chemical weathering in view of the upward increasing trend  
128 of BD1400/BD1900 (Liu et al., 2021b). However, a weathering succession may include  
129 sections formed from protoliths with systematic variations in minerals and/or organics,  
130 which may affect absorption features at ~1400 and ~1900 nm (Liu et al., 2021a; Tan et

131 al., 2022). Therefore, whether the band depth of the VNIR absorption and their ratios  
132 are due to chemical weathering still remains an open question, and a more reliable and  
133 quantitative correlation should be defined to interpret the genesis of compositional  
134 stratigraphy on the Mars.

135 The correlation between VNIR spectral features and weathering intensity of basaltic  
136 weathering succession can be quantified using different stages of kaolinized nontronite,  
137 whose OH and H<sub>2</sub>O variations can be quantitatively analyzed by thermogravimetric  
138 analysis (TG). In the present study, the transformation of nontronite to kaolinite was  
139 modeled experimentally, avoiding the influences of other minerals and organics in  
140 natural samples. The kaolinized nontronite samples with different OH and H<sub>2</sub>O contents  
141 were characterized using a combination of X-ray diffraction (XRD), scanning electron  
142 microscopy (SEM), TG and VNIR. The relationships between OH and BD1400, H<sub>2</sub>O  
143 content and BD1900, and the suitability of BD1400/BD1900 for characterizing  
144 weathering intensity (OH/H<sub>2</sub>O) were quantitatively investigated. The obtained dataset  
145 allows us to better interpret the near-infrared remote sensing data from Mawrth Vallis  
146 on Mars and discuss the genesis of compositional stratigraphy. Our study provides a  
147 quantitative correlation between VNIR parameters and weathering intensities of  
148 basaltic weathering successions. The obtained results shed light on whether or not  
149 compositional stratigraphy is related to top-down chemical weathering, which is critical  
150 to understanding the climate and atmospheric conditions of the early Mars.

151

## 152 **2 Sample preparation**

153 A series of kaolinized nontronite samples were prepared by converting nontronite  
154 to kaolinite with different experimental durations, according to the experiment of Li et  
155 al. (2020). The light green colored raw nontronite is from the Uley Graphite Mine in  
156 South Australia and is described as  $N_{Au}$ , and the chemical formula can be denoted as  
157  $M^{+1.05} [Al_{0.26}Fe_{3.71}Mg_{0.03}] [Si_{6.97}Al_{1.03}] O_{20} (OH)_4$  (Ding & Frost, 2002; Frost et al.,  
158 2002). In this study, 0.5 g of  $N_{Au}$  was added to 20 mL of 0.1 mol L<sup>-1</sup> AlCl<sub>3</sub> solution and  
159 transferred to a 250 mL para-phenylene lined autoclave. Given that the duration of these  
160 transformations at room temperature may exceed the experimentally observable  
161 duration, we performed the transformation experiments at 250 °C for 6, 12, 18, 24, 36,  
162 48, 96, and 144 hrs to accelerate the transformation of nontronite to kaolinite (Li et al.,  
163 2020). The obtained products were washed with deionized water and centrifuged at  
164 11,000 rpm, and dried at 80 °C for 24 hrs, denoted as  $N_{Au-X}$ , where X refers to the  
165 experimental duration.

166

## 167 **3 Analytical Methods**

168 *X-ray diffraction (XRD)*. XRD analysis was performed on a Rigaku MiniFlex-600  
169 X-ray diffractometer with Cu/K $\alpha$  radiation and a Ni filter operating at a current of 15  
170 mA and voltage of 40 kV. The specimens were scanned from 3° to 70° (2 $\theta$ ) with a step  
171 size of 0.02 ° and a scanning rate of 10 °/min.

172 *Scanning electron microscopy (SEM)*. SEM images were obtained using an  
173 Analytical Scanning Electron Microscope (TESCAN MIRA 3) equipped with an energy

174 dispersive X-ray spectrometer (EDS) operated at an accelerating voltage of 20 kV and  
175 working distance (WD) of 15-16 mm.

176 *Thermogravimetric analysis (TG).* TG analyses were conducted on a Netzsch STA  
177 409PC instrument at the Key Laboratory of Mineralogy and Metallogeny of the  
178 Guangzhou Institute of Geochemistry, Chinese Academy of Sciences (GIGCAS).  
179 About 10 mg of the samples were heated in a corundum crucible. The samples were  
180 heated from 30 to 1000 °C at a heating rate of 10 °C/min in an N<sub>2</sub> atmosphere (60 cm<sup>3</sup>  
181 /min). The differential thermogravimetric (DTG) curves were derived from the TG data.

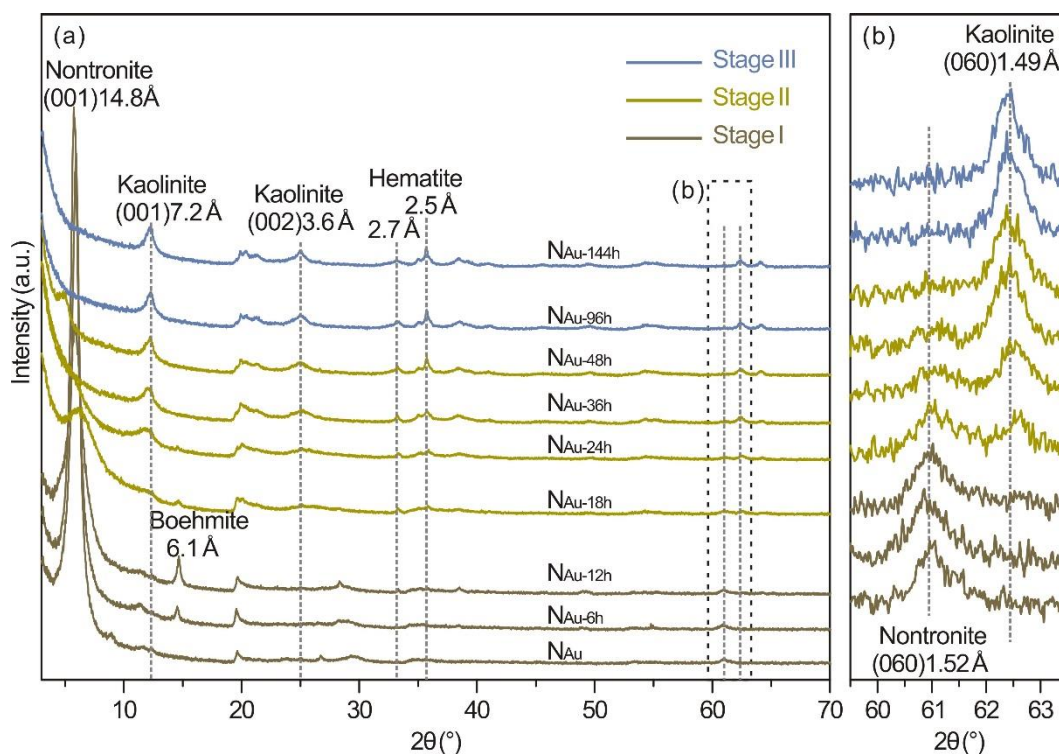
182 *Visible/near infrared (VNIR) reflectance spectroscopy.* VNIR reflectance  
183 spectroscopy spectra were acquired at wavelengths from 350–2500 nm using an  
184 Analytical Spectral Devices (ASD) Terraspec-4 spectrometer at University of Hong  
185 Kong (Hong Kong, China), and the spot size is ~20 mm. Reflectance was measured  
186 relative to a white reflectance standard Spectral on plate. One hundred scan acquisitions  
187 were set to yield an average spectrum for each measurement to improve the signal-to-  
188 noise ratio. The ASD spectral files were splice corrected and averaged using the  
189 ViewSpecPro (version 6.0) software and then converted to ASCII format. Spectral  
190 parameters (e.g., band depth) were calculated according to Liu (2021a, 2021b) and  
191 Viviano-Beck (2014).

192

193 **4 Results**

194 4.1. Phases and morphology of different stages of kaolinized nontronite

195 Based on the mineral composition and transformation duration of nontronite to  
196 kaolinite, the samples can be divided into three stages. The Stage I samples ( $N_{Au}$ ,  $N_{Au-6h}$   
197 and  $N_{Au-12h}$ ) were dominated by nontronite, which corresponded to the infantile  
198 weathering stage of nontronite. The Stage II samples ( $N_{Au-18h}$ ,  $N_{Au-24h}$ ,  $N_{Au-36h}$  and  $N_{Au-48h}$ )  
199 were composed of nontronite, hematite and kaolinite, corresponding to the  
200 intermediate weathering stage of nontronite. The Stage III samples ( $N_{Au-96h}$  and  $N_{Au-144h}$ )  
201 consisted of kaolinite, hematite, and little nontronite, corresponding to the  
202 advanced weathering stage of nontronite.



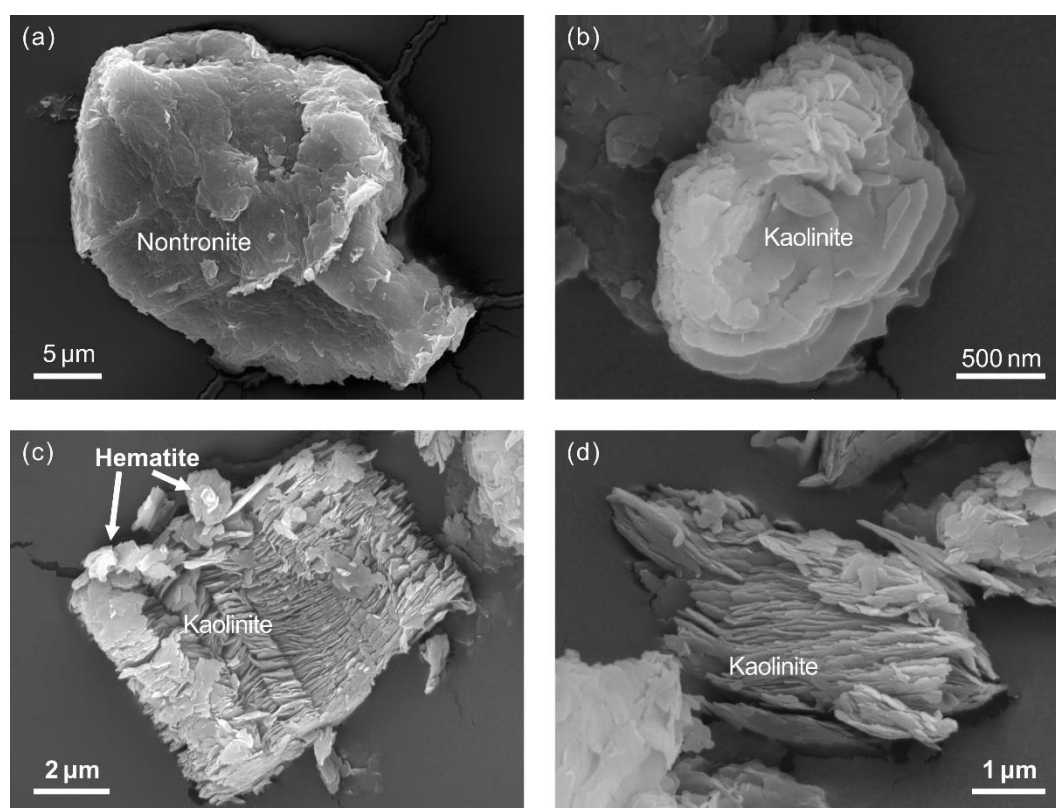
203 **Figure 2.** (a) XRD patterns ( $CuK\alpha$ ) of different stages of kaolinized nontronite; (b) Enlarged XRD  
204 patterns of (060) region from the dotted rectangle in (a). Note, the samples are divided into Stage I  
205 ( $N_{Au}$ ,  $N_{Au-6h}$  and  $N_{Au-12h}$ ), Stage II ( $N_{Au-18h}$ ,  $N_{Au-24h}$ ,  $N_{Au-36h}$  and  $N_{Au-48h}$ ) and Stage III ( $N_{Au-96h}$  and  
206  $N_{Au-144h}$ ) based on the mineral composition and the duration of experiment.  
207

208 The Stage I samples showed characteristic reflections at  $\sim 14.8$  and  $\sim 1.52$  Å (Figure  
209 2), corresponding to the (001) and (060) reflections of nontronite (Fernandez-Caliani et  
210 al., 2004; Kawi & Yao, 1999). SEM observations showed that the Stage I samples  
211 exhibited plate-like morphology with jagged grain boundaries (Figure 3a), which is a  
212 typical feature of smectite group minerals (Zhang et al., 2017). The Stage I samples  
213 showed gradually weakening reflections of nontronite (e.g., 1.52 Å) with increasing  
214 duration of the experiment (Figure 2b), indicating a decrease in nontronite content. In  
215 addition, N<sub>Au-6h</sub> and N<sub>Au-12h</sub> showed characteristic reflections of boehmite at  $\sim 6.1$  Å  
216 (Figure 2a), a common phase precipitated from Al<sup>3+</sup>-bearing solution (Li et al., 2020).

217 Compared to the Stage I samples, the Stage II samples showed three additional  
218 reflections at  $\sim 7.2$ ,  $\sim 3.6$  and  $\sim 1.49$  Å (Figure 2), corresponding to the (001), (002) and  
219 (060) reflections of kaolinite, respectively. Accordingly, the reflections of nontronite  
220 gradually decreased at  $\sim 14.8$  and  $\sim 1.52$  Å. It is noteworthy that the Stage II samples  
221 also displayed two reflections at d-values of  $\sim 2.7$  and  $\sim 2.5$  Å (Figure 2a), corresponding  
222 to the (104) and (110) reflections of hematite, respectively. Well crystallized kaolinite  
223 and hematite were ubiquitous in the Stage II (Figures. 3b-c). As the transformation of  
224 nontronite to kaolinite progressed, the reflection intensities of both hematite and  
225 kaolinite gradually increased (Figure 2), indicating an increase in their abundance.  
226 Moreover, the grain size of kaolinite in the Stage II samples gradually increased from  
227  $\sim 2$  μm (N<sub>Au-24h</sub>) to  $\sim 6$  μm (N<sub>Au-48h</sub>) (Figures. 3b-c).

228 Compared to the Stage II samples, the Stage III samples showed prominent  
229 reflections of kaolinite at  $\sim 7.2$ ,  $\sim 3.6$  and  $\sim 1.49$  Å, and hematite at  $\sim 2.7$  and  $\sim 2.5$  Å, and

230 these reflections were sharper compared to the Stage II samples (Figure 2). In contrast,  
231 the reflections of nontronite were negligible (Figure 2), indicating that the Stage III  
232 samples were composed mainly of kaolinite and hematite with little nontronite. The  
233 (060) reflection of kaolinite occurred at 1.49 Å (Figure 2b), which corresponded to the  
234 Al-infilling oxygen octahedral sheets of kaolinite. Accordingly, the Stage III samples,  
235 e.g., N<sub>Au-96h</sub>, showed well-crystallized kaolinite layers (Figure 3d).



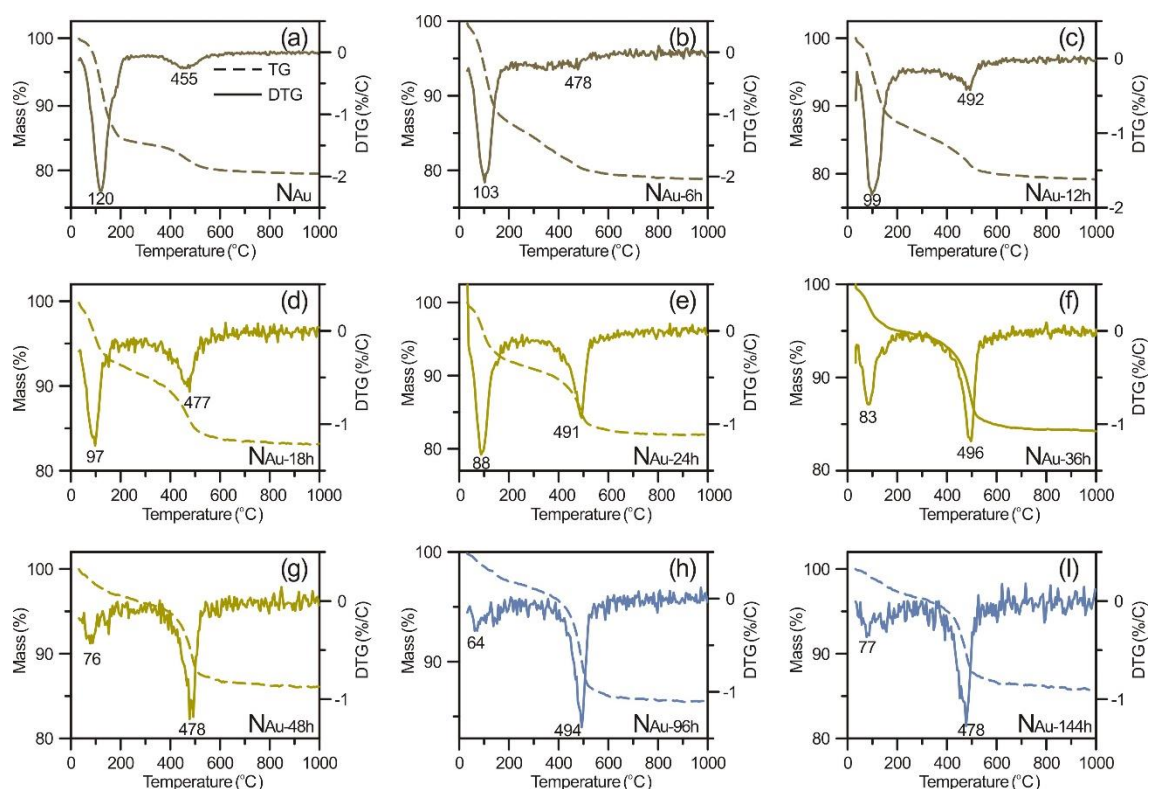
236  
237 **Figure 3.** Scanning electron microscopic images of different stages of kaolinized nontronite. (a)  
238 nontronite particle in sample N<sub>Au</sub>; (b) kaolinite particle in sample N<sub>Au-24h</sub>; (c) kaolinite and hematite  
239 particle in sample N<sub>Au-48h</sub>; and (d) kaolinite particle in sample N<sub>Au-96h</sub>.

240

#### 241 4.2 Hydroxyl (OH) and water molecule (H<sub>2</sub>O) contents

242 Nontronite generally showed significant mass losses in the range from room  
243 temperature to ca. 300 °C, which originates from loss of interlayer water associated with

244 interlayer cations (*e.g.*, K<sup>+</sup>, Na<sup>+</sup>, and Ca<sup>2+</sup>). Significant mass losses at temperature above  
 245 300 °C can be attributed to dehydroxylation of clay minerals (He et al., 2017; Li et al.,  
 246 2020; Zhang et al., 2017). Accordingly, the OH and H<sub>2</sub>O contents of the three stages of  
 247 samples can be quantified using the TG analysis based on the mass loss caused by  
 248 dehydration and dehydroxylation (Figure 4).



249 **Figure 4.** TG and DTG curves collected from different stages of kaolinized nontronite. The solid  
 250 line is the curves of DTG and the dashed line is the curves of TG. The colors of TG and DTG curves  
 251 correspond to the sample stage colors in Figure 2.  
 252

253

254 The TG and DTG curves of the Stage I samples showed two major mass losses at  
 255 100–120 °C and 455–500 °C (Figures 4a-c), corresponding to the dehydration and  
 256 dehydroxylation temperatures of nontronite, respectively (Ding & Frost, 2002). In  
 257 general, the Stage I samples had a higher dehydration temperature (Figures 4a-c). The

258 Stage I samples generally lost about 15 wt.% mass at 30–300 °C due to dehydration,  
259 and about 6 wt.% mass at 300–700 °C due to dehydroxylation (Figures 4a-c).

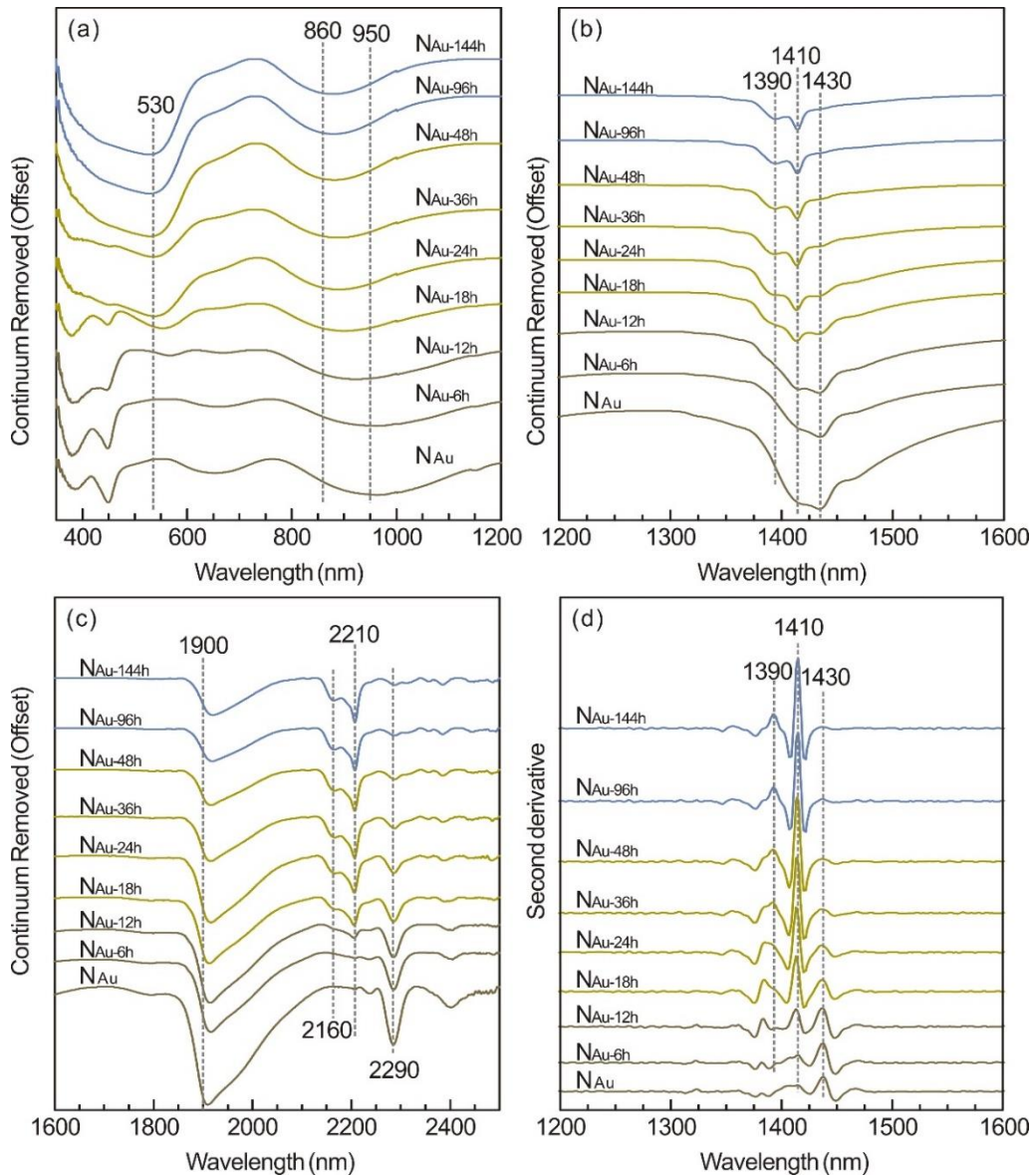
260 The Stage II samples generally had a lower dehydration temperature compared to  
261 the Stage I samples. In particular, the TG and DTG curves of the Stage II samples  
262 showed significant mass loss at about 90 and 500 °C (Figures 4d-g), corresponding to  
263 the dehydration and dehydroxylation temperatures of the nontronite and kaolinite  
264 mixture. As the transformation of nontronite to kaolinite progressed, the dehydration  
265 temperatures gradually decreased from 97 to 76 °C and the main dehydroxylation  
266 temperature occurred at ~500 °C. Calculations showed that the mass losses of  
267 dehydration were 4–10 wt.% and the mass losses of dehydroxylation were 7–10 wt.%  
268 (Figures 4d-g).

269 The Stage III samples had different dehydration temperatures and mass losses  
270 during dehydration and dehydroxylation compared to the Stage II samples. The TG and  
271 DTG curves of the samples from the Stage III showed two prominent mass loss  
272 temperatures at ~64 and ~500 °C (Figures 4h-I), corresponding to the dehydration and  
273 dehydroxylation of kaolinite, respectively. In addition, the samples from the Stage III  
274 exhibited ~3 wt.% mass loss due to dehydration at 30–300 °C and ~10 wt.% mass losses  
275 due to dehydroxylation at 300–700 °C (Figures 4h-I).

#### 276 4.3 VNIR spectra of kaolinized nontronite

277 VNIR spectroscopy (350–2500 nm) includes the visible (350–1000 nm) and near  
278 infrared (1000–2500 nm) regions (Hunt, 1977; Hunt & Ashley, 1979). In this study, the  
279 absorption bands at 350–1000 nm are likely due to the electronic transitions of Fe<sup>3+</sup> in

280 nontronite and hematite. The absorption bands at 1000–2500 nm corresponded to the  
 281 overtone and combination of water and metal-OH (metal=Al, Fe and Mg) in nontronite  
 282 and kaolinite (Bishop et al., 2002, 2008; Cuadros et al., 2016; Fox et al., 2021).



283  
 284 **Figure 5.** Visible/near-infrared reflectance spectra of different stages of kaolinized nontronite. (a)  
 285 Continuum-removed reflectance spectra of Fe-related bands within the range of 350-1200 nm; (b)  
 286 Continuum-removed reflectance spectra of OH at the band of 1200–1600 nm; (c) Continuum-  
 287 removed reflectance spectra at the band of 1600–2500 nm, and show a decrease trend of the  
 288 absorption band at 1900 nm (d) Second derivative curves of OH at the band of 1200–1600 nm and  
 289 show an increase trend of the absorption band at 1410 nm. The spectra have been offset for clarity  
 290 but are shown on a common scale for band intensity comparison. The colors of spectral curves  
 291 correspond to the sample stage colors, referring to figure 2.

292 Spectra of the Stage I samples showed characteristic absorptions of nontronite at  
293 ~950, ~1430, ~1900 and ~2290 nm (Figure 5a). The absorption at ~950 nm  
294 corresponded to the Fe<sup>3+</sup> electronic transitions of nontronite. The absorption at ~1430  
295 nm was the first overtone of the Fe<sup>3+</sup>Fe<sup>3+</sup>-OH stretching of nontronite. The band at  
296 ~1900 nm corresponded to a combination of stretching and bending vibrations of the  
297 interlayer H<sub>2</sub>O. Furthermore, the absorption at ~2290 nm was from the combination of  
298 stretching and bending vibrations of Fe<sup>3+</sup>Fe<sup>3+</sup>-OH and was the diagnostic absorption of  
299 nontronite (Bibring et al., 2005; Bishop et al., 2008; Ehlmann et al., 2009). The  
300 absorption depth at ~2290 nm of the samples gradually decreased with progressive  
301 transformation of nontronite to kaolinite (Figure 5c).

302 The Stage II samples showed additional characteristic absorptions at ~1390, ~1410,  
303 ~2160 and ~2210 nm (Figures 5b-c). The absorptions at ~1390 and ~1410 nm were  
304 derived from the first overtone of AlAl-OH stretching, and the absorptions at ~2160  
305 and ~2210 nm can be attributed to the combination of stretching and bending vibrations  
306 of AlAl-OH in kaolinite. The Stage II samples also showed characteristic absorption of  
307 hematite at ~530 and ~860 nm, which can be attributed to electron transitions from Fe<sup>3+</sup>.  
308 As the transformation of nontronite to kaolinite progressed, the Stage II samples  
309 showed a gradual increase in the absorption intensity of hematite at ~530 nm and  
310 kaolinite at ~1410 nm (Figures 5a & d). Correspondingly, the absorption of nontronite,  
311 *e.g.*, at ~1430 nm, was gradually weakened (Figure 5d).

312 The absorption of nontronite (*e.g.*, ~1430 nm) in the Stage III samples was further  
313 weakened and disappeared (Figure 5d), while the absorption of kaolinite and hematite

314 was gradually enhanced (Figure 5). Specifically, the Stage III samples showed the  
315 absorption of hematite at ~530 and ~860 nm and that of kaolinite at ~1390, ~1410,  
316 ~2160 and ~2210 nm.

317

## 318 **5 Discussion**

### 319 5.1. Transformation of nontronite to kaolinite in basaltic weathering successions

320 Weathering of basalt is dominated by the surface process of top-down leaching,  
321 which leads to decomposition of rock-forming minerals (*e.g.*, olivine and pyroxene)  
322 and subsequent formation of secondary minerals (*e.g.*, nontronite and kaolinite) (Liu et  
323 al., 2021a; Nahon et al., 1982). Chemical reactions between water and basalt tend to  
324 convert anhydrous materials, *e.g.*, olivine and pyroxene, to the clay mineral nontronite  
325 of type 2:1 at the stage of early weathering, by leaching composition elements (*e.g.*, Ca,  
326 Mg and Si) and inducing OH and H<sub>2</sub>O (Cuadros & Michalski, 2013; Ehlmann et al.,  
327 2011b; Nahon et al., 1982; Wilson, 2004). H<sub>2</sub>O tends to form complexes with interlayer  
328 cations (*e.g.*, K<sup>+</sup>, Na<sup>+</sup>, Ca<sup>2+</sup>) within the interlayer sites of nontronite, whereas OH is  
329 likely bound to the Al/Fe/Mg-O octahedral sheet of nontronite (Cuadros & Michalski,  
330 2013).

331 In the context of the weathering profile, nontronite is a transient phase that forms  
332 in weathered rocks (Wilson, 2004). Basaltic weathering successions generally show a  
333 gradual increase in the amount of kaolinite from bottom to top due to progressive  
334 weathering, as evidenced by the transitional zones containing different proportions of  
335 nontronite and kaolinite in basaltic weathering successions formed under warm

336 climates (Gaudin et al., 2011; Prudencio et al., 2002). During the transformation of  
337 nontronite to kaolinite, more OH is incorporated into the clay mineral structure by  
338 hydrolysis, while H<sub>2</sub>O in the interlayer, cations, and Si-O tetrahedral sheets tend to be  
339 gradually leached (Li et al., 2020). As a result, the transformation of nontronite to  
340 kaolinite mainly involves changes in the OH/H<sub>2</sub>O and Si/Al ratios in the clay minerals,  
341 which are essentially positively correlated with the weathering intensity of a basaltic  
342 weathering succession (Liu et al., 2021a).

343

## 344 5.2. Change of H<sub>2</sub>O and OH content in the transformation of nontronite to kaolinite

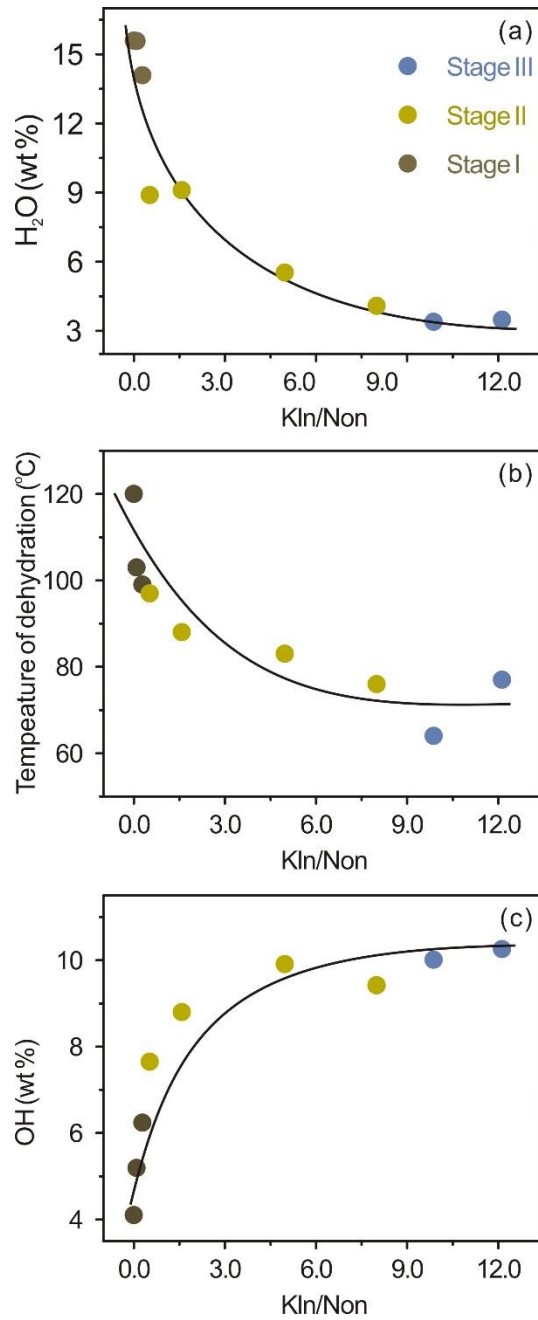
345 Sustained leaching of Si from nontronite lowers the Si/Al ratio in the mineral-water  
346 reaction system, facilitating the transformation of nontronite to kaolinite. In the present  
347 study, a similar transformation process is modeled experimentally by lowering the Si/Al  
348 ratio of the nontronite-water reaction system with external Al<sup>3+</sup>. With increased reaction  
349 time, the initial mineral nontronite is gradually transformed into a mixture of nontronite  
350 and kaolinite, and finally to kaolinite (Figures 2 & 3), which is consistent with clay  
351 mineral transformation in a basaltic weathering succession (Gaudin et al., 2011; Liu et  
352 al., 2021a; Prudencio et al., 2002).

353 In the transformation of nontronite to kaolinite, nontronite is the main host of H<sub>2</sub>O  
354 bound with its interlayer cations, whereas kaolinite contains few interlayer cations and  
355 H<sub>2</sub>O (Cuadros, 1997; Ding & Frost, 2002; Fernandez-Caliani et al., 2004; Fox et al.,  
356 2021; Pineau et al., 2022). Analysis of TG shows that the H<sub>2</sub>O concentration of the  
357 transformation products gradually decreases from ~15 wt.% in the Stage I samples to

358 4–10 wt.% in the Stage II samples and to ~3 wt.% in Stage III samples (Figure 4 and  
359 Figure 6a). Furthermore, the dehydration temperature systematically shifts to lower  
360 temperatures as the transformation of nontronite to kaolinite progresses, from 100–  
361 120 °C in the Stage I samples to ~76–97 °C in the Stage II samples, and finally to ~64 °C  
362 in Stage III samples (Figure 4 and Figure 6b). The decrease in dehydration temperature  
363 indicates that less energy is required to break the hydrogen bond between the H<sub>2</sub>O  
364 molecules in the nontronite (Madejov á et al., 2002), corresponding to a decrease in the  
365 abundance of nontronite in the transformation products (Figure 2&3). Thus, the  
366 decrease in H<sub>2</sub>O content is consistent with the abundance of nontronite during the  
367 progressive transformation of nontronite into kaolinite.

368 The transformation of nontronite to kaolinite also leads to significant changes in  
369 the OH content of the different stages of kaolinized nontronite. The kaolinite has 8  
370 hydroxyl groups per complete structural formula, whereas nontronite has only 4  
371 hydroxyl groups (Cuadros et al., 2019; Li et al., 2020). Thus, one half of the Si-O  
372 tetrahedral sheets should be lost and hydroxyl groups induced when nontronite  
373 transforms to kaolinite. The analyses of TG show that the content of OH gradually  
374 increases from ~6 wt.% to ~10 wt.% as the transformation of nontronite to kaolinite  
375 progresses (Figure 4 and Figure 6c). Thus, the increase in OH content is consistent with  
376 the abundance of kaolinite during the progressive transformation of nontronite into  
377 kaolinite.

378



379

380 **Figure 6.** Change of H<sub>2</sub>O and OH content in the transformation of nontronite to kaolinite. (a) The  
 381 mass losses of dehydrations of different stages of nontronite → kaolinite transformation products;  
 382 (b) The dehydrations temperature of different stages of nontronite → kaolinite transformation  
 383 products; and (c) The mass losses of dehydroxylations in different stages of nontronite → kaolinite  
 384 transformation products.

385

### 386 5.3. Spectral proxies for kaolinized nontronite

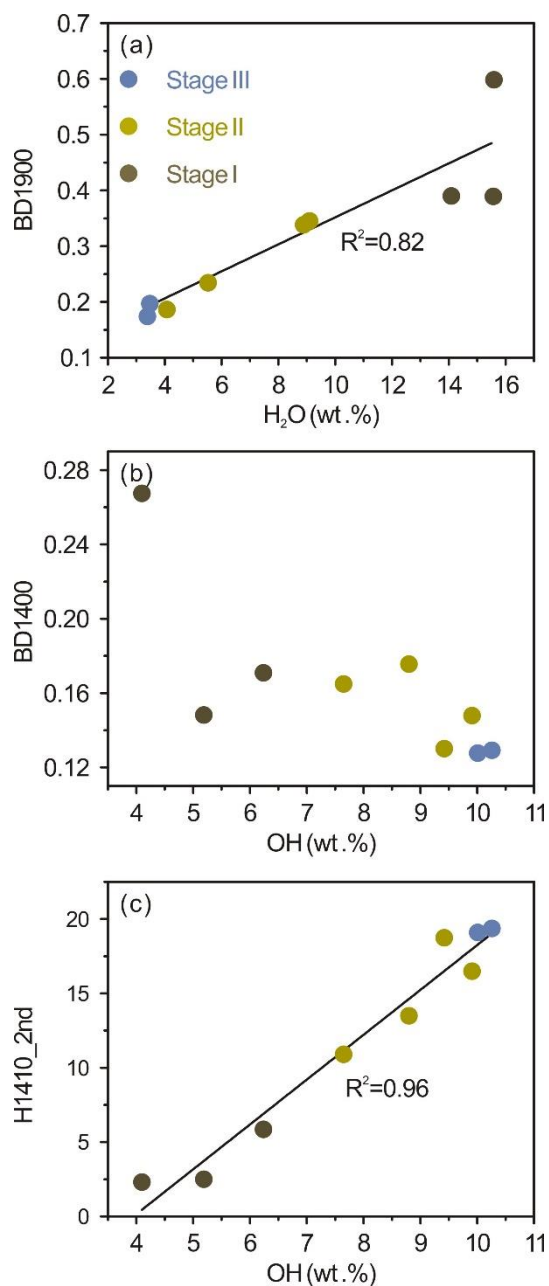
387 Previous studies suggest that interlayer cations and the amount of interlayer water

388 determine the VNIR spectral features at band of 1900 nm (Bishop et al., 1994).

389 Nevertheless, interlayer cations of clay minerals only have indirect effects on ~1900  
390 nm absorption by affecting the amount of H<sub>2</sub>O molecules bound on them (Bishop et al.,  
391 1994). In the present study, the band depth at ~1900 nm (BD1900) gradually decreases  
392 as the transformation of nontronite to kaolinite progresses (Figure 5c). Remarkably,  
393 BD1900 shows a positive linear correlation ( $R^2=0.82$ ) with the H<sub>2</sub>O content in the  
394 different stages of kaolinized nontronite (Figure 7a). Since nontronite is the major host  
395 of H<sub>2</sub>O, the BD1900 can serve as an effect spectral proxy to quantify the abundance of  
396 nontronite in the transformation products.

397 The band position of OH absorption at 1400 nm is affected by the electronegativity  
398 and ionic radius of the octahedral cations (Mart ínez-Alonso et al., 2002). The VNIR  
399 absorption at ~1400 nm possible includes three bands originating from metal-OH  
400 vibrations in kaolinite and nontronite, *i.e.*, 1390 nm, 1410 nm, and 1430 nm (Figure  
401 5b&d). The band at 1390 nm originates from the first overtone of inner-surface  
402 hydroxyl groups' stretching vibration of AlAl-OH in kaolinite, the band at 1410 nm  
403 originated from the first overtone of inner hydroxyl groups' stretching vibration of  
404 AlAl-OH in kaolinite (Tan et al., 2022), and the band at near 1430 nm derived from  
405 stretching vibration of Fe<sup>3+</sup>Fe<sup>3+</sup>-OH in nontronite (Bishop et al., 2008; Ehlmann et al.,  
406 2009). Therefore, the band depths at 1390 and 1410 nm tend to increase, while the band  
407 depth at 1430 nm decreases as the transformation of nontronite to kaolinite progresses  
408 (Figures 5b & d). As a result, the band depth at ~1400 nm (BD1400) poorly correlates  
409 with the concentrations of OH in the different stages of kaolinized nontronite, due to  
410 the interference of the three bands (Figure 7b). In contrast, the spectral proxy

411 H1410\_2nd (height of second derivative curves at the band of 1410 nm) gradually  
 412 increases (Figure 5d) and shows a positive linear correlation ( $R^2=0.96$ ) with the content  
 413 of OH in the kaolinized nontronite (Figure 7c).



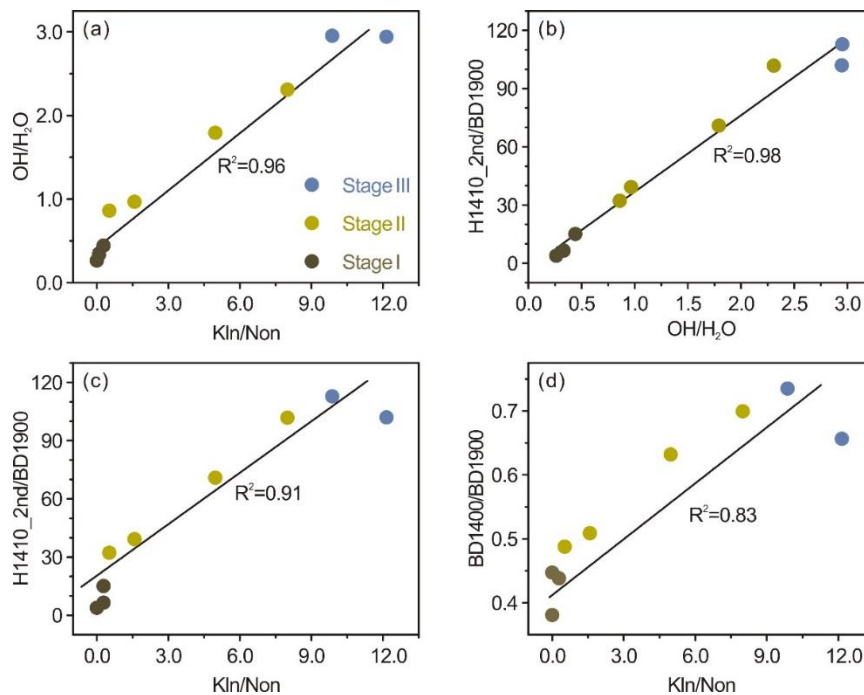
414  
 415 **Figure 7.** Spectral proxies of H<sub>2</sub>O and OH content in the nontronite → kaolinite transformation. (a)  
 416 Plots of the spectral parameters BD1900 versus H<sub>2</sub>O content; (b) Plots of the spectral parameters  
 417 BD1400 versus OH content; and (c) Plots of the spectral parameters H1410\_2nd versus OH content.  
 418

#### 419 5.4 Spectral proxies for weathering intensity of basaltic successions

420 Progressive chemical weathering of terrestrial basalt results in replacement of  
421 nontronite with kaolinite, leading to an increase in OH content and a concomitant  
422 decrease in H<sub>2</sub>O content (Figure 4&6). Thus, the ratio of OH to H<sub>2</sub>O content is  
423 essentially related to the weathering intensity of a basaltic weathering succession and  
424 increases gradually (Figure 8a). The present study has shown that the content of H<sub>2</sub>O  
425 and OH can be quantitatively assessed by the spectral proxies BD1900 (Figure 7a) and  
426 H1410\_2nd (Figure 7c), respectively. In particular, the ratio of H1410\_2nd to BD1900  
427 (H1410\_2nd/BD1900) shows a strong positive correlation ( $R^2=0.98$ ) with weathering  
428 intensity (OH/H<sub>2</sub>O, Figure 8b) and the abundance ratio of kaolinite to nontronite  
429 (Kln/Non, Figure 8c). Therefore, the weathering intensity of a basaltic weathering  
430 succession can be well estimated by the spectral proxy H1410\_2nd/BD1900 (Figure 8c;  
431  $R^2=0.91$ ).

432 Specifically for CRISM spectra collected from the surface of Mars, the data set has  
433 a relatively low signal-to-noise ratio (Pineau et al., 2022; Zhang et al., 2022) and is  
434 characterized by weak and broad absorption (Cuadros et al., 2016). As a result, the  
435 absorption at the 1390 nm, 1410 nm, and 1430 nm can hardly be resolved, and it is  
436 unreasonable to use H1410\_2nd/BD1900 to quantitatively constrain the weathering  
437 intensities of a basaltic weathering succession on Mars. Nevertheless, photooxidation  
438 may have affected the Fe-clay minerals formed near the surface and caused the  
439 absorption of Fe<sup>3+</sup>Fe<sup>3+</sup>-OH to disappear at ~1400 nm (Rivera Banuchi et al., 2022). The  
440 absorption band at ~1400 nm is likely caused by AlAl-OH of kaolinite on Mars, so

441 BD1400 is likely effective for characterizing the OH content of kaolinite on Mars.  
 442 Given that the ratio of BD1400 to BD1900 (BD1400/BD1900) also demonstrates a  
 443 reasonable positive correlation with the abundance ratio of kaolinite to nontronite  
 444 (Figure 8d;  $R^2=0.83$ ), the BD1400/BD1900 can serve as a good indication of  
 445 weathering intensity in the basaltic weathering succession on Mars.



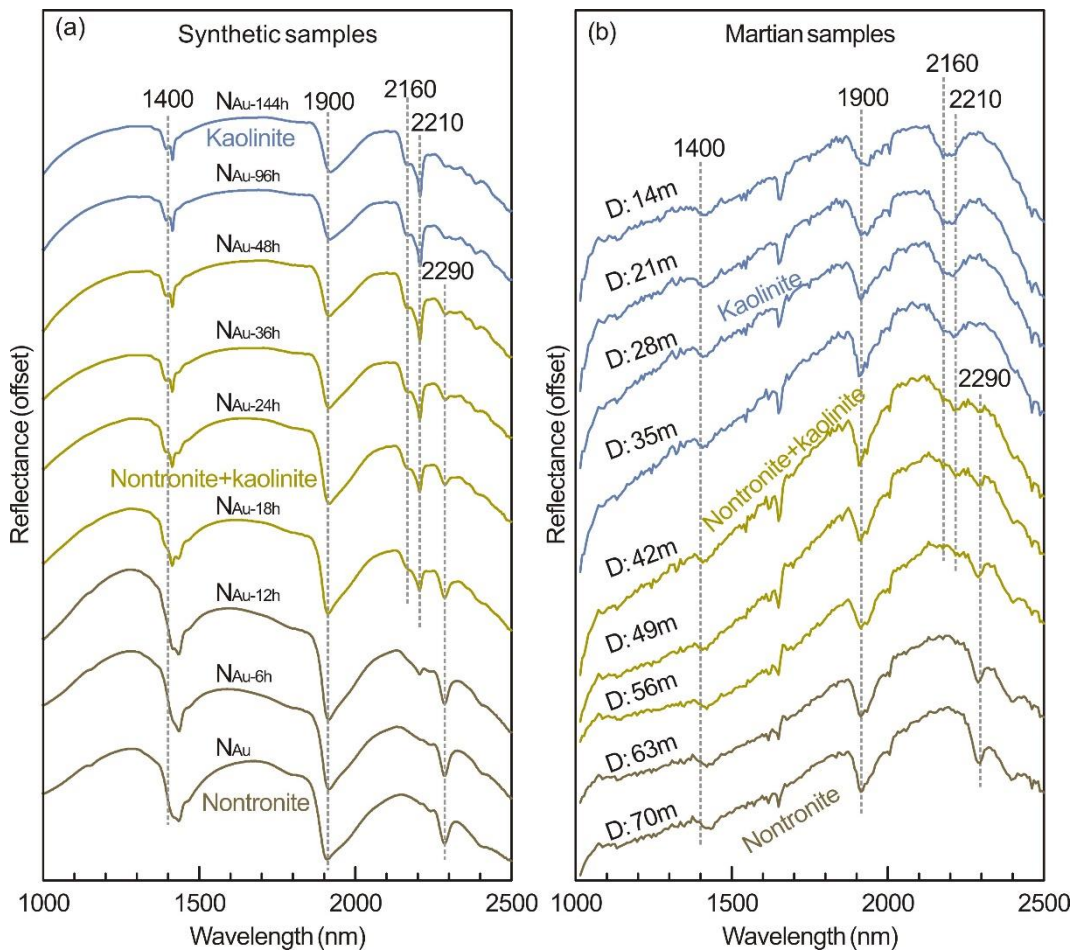
446 **Figure 8.** Spectral proxies for weathering intensity of basaltic succession. (a) Plots of the abundance  
 447 ratio of OH to H<sub>2</sub>O (OH/H<sub>2</sub>O) versus the abundance ratio of kaolinite (Kln) to nontronite (Non)  
 448 (Kln/Non); (b) Plots of H1410\_2nd/BD1900 versus the weathering intensity proxy OH/H<sub>2</sub>O; (c)  
 449 Plots of H1410\_2nd/BD1900 versus Kln/Non and (d) Plots of BD1400/BD1900 versus Kln/Non.

451

## 452 5.5. Analogue spectra of the compositional stratigraphy on Mars

453 The main debate about the genesis of compositional stratigraphy on the Martian  
 454 surface is whether the clay minerals changed through chemical weathering (Bibring et  
 455 al., 2006; Bishop et al., 2018; Carter et al., 2015; Ehlmann et al., 2013; Liu et al., 2021b;  
 456 Ye & Michalski, 2021) or formed by deposition of various sediments (Bishop et al.,

457 2020; Ehlmann et al., 2013; Lowe et al., 2020; Michalski et al., 2013). This study  
 458 provides spectral parameters collected from different stages of kaolinized nontronite,  
 459 *e.g.*, BD1400, BD1900 and BD1400/BD1900, to investigate the content of OH, H<sub>2</sub>O,  
 460 and weathering intensity of the different units consisting compositional stratigraphy on  
 461 Mars, which could provide crucial clues to the genesis of compositional stratigraphy.



462  
 463 **Figure 9.** Comparison between the reflectance spectra of the nontronite → kaolinite transformation  
 464 products with the CRISM spectra collected from a compositional stratigraphy on Mars. (a) The  
 465 spectra of sample N<sub>Au</sub> and its transformed products; (b) the CRISM spectra from the different depths  
 466 of a compositional stratigraphy on Mars (the data on which this figure is based are available in Liu  
 467 et al., 2021b), and D is depth of the thick clays profile.

468

469 Spectra from the α1 zone of the compositional stratigraphy on Mars show

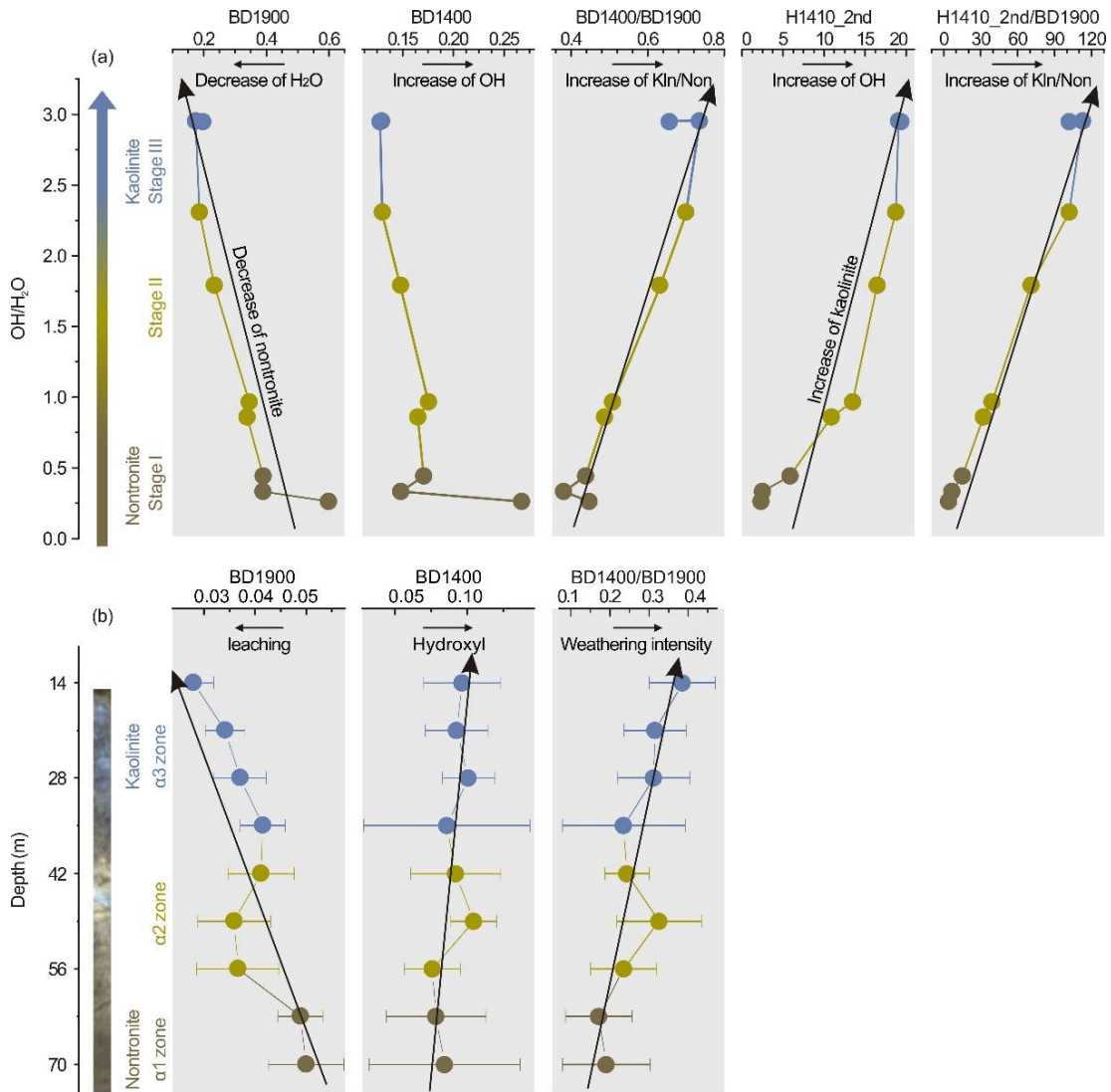
470 absorption bands at ~1400, ~1900, and ~2290 nm (Figure 9b). The band positions of

471 these absorptions are consistent with those of nontronite from Stage I samples in the  
472 laboratory (Figure 9a) and the absorption at ~2290 nm is the diagnostic absorption of  
473 nontronite (Bibring et al., 2005), suggesting that nontronite, is the dominant mineral in  
474 the  $\alpha_1$  zone.

475 In the  $\alpha_2$  zone of the compositional stratigraphy, the spectra have absorptions at  
476 ~1400, ~1900, ~2200 and ~2290 nm (Figure 9b). The band positions of these  
477 absorptions are consistent with those of the Stage II kaolinized nontronite (Figure 9a).  
478 The band asymmetry of the ~2200 absorption gradually shift toward the short  
479 wavelength side, indicating the presence of kaolinite (Bibring et al., 2005). As a result,  
480 the  $\alpha_2$  zone of the compositional stratigraphy represent a mixture of nontronite and  
481 kaolinite.

482 Moreover, BD1900 gradually decreases while BD1400 gradually increases from  
483 bottom to top in the  $\alpha_2$  zone (Figure 10b), which is exactly consistent with the  
484 transformation of the samples of the Stage II (Figure 10a). This shows that hydroxyl  
485 and leaching gradually increase upward. In addition, BD1400/BD1900 shows a  
486 consistent increasing trend from the bottom to top in the Martian profile (Figure 10b),  
487 which is accordant with the progressive transformation of nontronite to kaolinite  
488 (Figure 10a). These variation trends in spectral proxies along the compositional  
489 stratigraphy from bottom to top reflect the gradual decomposition of nontronite and  
490 formation of kaolinite with increasing weathering intensity, by relating to the  
491 experimentally modeled transformation of nontronite to kaolinite.

492



493

494 **Figure 10.** Variation trends of the spectral parameters of different stages of kaolinized nontronite  
 495 and a compositional stratigraphy in the Mawrth Vallis region, Mars. (a) Variation of the spectral  
 496 parameters BD1900, BD1400, BD1400/BD1900, H1410\_2nd and H1410\_2nd/BD1900 in the  
 497 progressive transformation of nontronite to a mixture of nontronite and kaolinite, and finally to  
 498 kaolinite; (b) The variation of the spectral parameters BD1900, BD1400 and BD1400/BD1900  
 499 along the compositional stratigraphy on Mars (the data on which this figure is based are available  
 500 in Liu et al., 2021b).

501

502 The spectra from the α<sub>3</sub> zone show absorptions at ~1400 and ~1900 nm and a  
 503 doublet at ~2200 nm while the absorption at ~2290 nm disappears (Figure 9b). The  
 504 band positions of these absorptions are consistent with those of kaolinite from  
 505 experimentally modeled Stage III samples (Figure 9a). The doublet at ~2200 nm is the

506 diagnostic absorption of kaolinite, indicating that kaolinite becomes the dominant phase  
507 in the  $\alpha_3$  zone.

508 These observed variation trends in CRISM spectra reflect evolutionary features of  
509 both mineral composition and weathering intensity in the compositional stratigraphy of  
510 Mars (Figure 10). In particular, the variation trends of BD1900, BD1400 and  
511 BD1400/BD1900 continue from the  $\alpha_1$  zone to the  $\alpha_3$  zone in the compositional  
512 stratigraphy (Figure 10b), corresponding to a progressive conversion of nontronite to  
513 kaolinite by chemical weathering from top to bottom. Such continuous variation trends  
514 can hardly be achieved by the stratigraphic deposition of detrital phyllosilicate  
515 sediments, which are likely to exhibit irregular fluctuations in mineral composition and  
516 weathering intensity due to the unpredictable origin of the sediments and abrupt  
517 changes in protolithic minerals (Liu et al., 2021a; Tan et al., 2022). Thus, the  
518 compositional stratigraphy on Mars may have been formed by a top-down chemical  
519 weathering process. It is possible that Mars had a warm and wet climate capable of  
520 maintaining liquid water on the surface over geologic time and the compositional  
521 stratigraphy formed through the ongoing reaction between the liquid water and the  
522 primary minerals in basalt.

523

## 524 **6 Conclusions**

525 The transformation of nontronite to kaolinite is modeled experimentally and  
526 studied quantitatively using TG and VNIR to test the effectiveness of spectral proxies  
527 for mineral evolution and weathering intensity in a basaltic succession. Analysis of TG

528 shows that the H<sub>2</sub>O content gradually decreases, while OH gradually increases with the  
529 progressive transformation of nontronite to kaolinite. Thus the ratio of OH/H<sub>2</sub>O is  
530 positively correlated with the weathering intensity of a basaltic weathering succession.  
531 The present study demonstrates the effectiveness of BD1900, H1410\_2nd, H1410\_2nd  
532 /BD1900 and BD1400/BD1900 as spectral proxies for H<sub>2</sub>O content, OH content, and  
533 weathering intensity during the conversion of nontronite to kaolinite in a basaltic  
534 weathering succession. The obtained results allow us to reveal the genesis of  
535 compositional stratigraphy on Mars. The continuous trends of BD1900, BD1400 and  
536 BD1400/BD1900 indicate a progressive transformation of nontronite into a mixture of  
537 nontronite and kaolinite, and finally into kaolinite. Accordingly, the compositional  
538 stratigraphy on Mars may have been formed by a progressive chemical weathering  
539 process from top to bottom. Thus, the formation of the compositional stratigraphy  
540 suggests that Mars had a warm and wet climate that could hold liquid water on its  
541 surface over geologic time span.  
542

543 **Acknowledgement**

544 This work was financially supported by the National Natural Science Foundation of  
545 China (Grant No. 41921003; 41825003; 42072044), Department of Science and  
546 Technology of Guangdong Province (Grant No.2017GC010578), and the Science and  
547 Technology Planning Project of Guangdong Province, China (2020B1212060055).

548

549 **Data Availability Statement**

550 CRISM hyperspectral data and HiRISE image used in this work are available via the  
551 Planetary Data System (<https://pds.nasa.gov>). The mineralogical and VNIR  
552 spectroscopic characteristics of different stages of kaolinized nontronite is available in  
553 an external repository via <https://data.mendeley.com/datasets/ws34469r9x>.  
554 ViewSpecPro software (version 6.0) provided by ASD Inc. was used to process the  
555 original VNIR spectral data.

556

557

558 **References**

559 Bibring, J. P., Langevin, Y., Gendrin, A., Gondet, B., Poulet, F., Berthé M., et al. (2005).

560 Mars surface diversity as revealed by the OMEGA/Mars Express observations.

561 *Science*, 307(5715), 1576-1581. <https://doi.org/10.1126/science.1108806>

562 Bibring, J. P., Langevin, Y., Mustard, J. F., Poulet, F., Arvidson, R., Gendrin, A., et al.

563 (2006). Global mineralogical and aqueous Mars history derived from

564 OMEGA/Mars express data. *Science*, 312(5772), 400-404.

565 <https://doi.org/10.1126/science.1122659>

566 Bishop, J., Madejová J., Komadel, P., & Fröschl, H. (2002). The influence of structural  
567 Fe, Al and Mg on the infrared OH bands in spectra of dioctahedral smectites. *Clay*  
568 *Minerals*, 37(4), 607-616. <https://doi.org/10.1180/0009855023740063>

569 Bishop, J. L., Fairén, A. G., Michalski, J. R., Gago-duport, L., Baker, L. L., Velbel, M.  
570 A., et al. (2018). Surface clay formation during short-term warmer and wetter  
571 conditions on a largely cold ancient Mars. *Nature Astronomy*, 2(3), 260-213.  
572 <https://doi.org/10.1038/s41550-017-0377-9>

573 Bishop, J. L., Gross, C., Danielsen, J., Parente, M., Murchie, S. L., Horgan, B., et al.  
574 (2020). Multiple mineral horizons in layered outcrops at Mawrth Vallis, Mars,  
575 signify changing geochemical environments on early Mars. *Icarus*, 341, 113634.  
576 <https://doi.org/10.1016/j.icarus.2020.113634>

577 Bishop, J. L., Lane, M. D., Dyar, M. D., & Brown, A. J. (2008). Reflectance and  
578 emission spectroscopy study of four groups of phyllosilicates: Smectites,  
579 kaolinite-serpentines, chlorites and micas. *Clay Minerals*, 43(1), 35-54.  
580 <https://doi.org/10.1180/claymin.2008.043.1.03>

581 Bishop, J. L., Pieters, C. M., & Edwards, J. O. (1994). Infrared spectroscopic analyses  
582 on the nature of water in montmorillonite. *Clays and Clay Minerals*, 42(6), 702-  
583 716. <https://doi.org/10.1346/ccmn.1994.0420606>

584 Bristow, T. F., Grotzinger, J. P., Rampe, E. B., Cuadros, J., Chipera, S. J., Downs, G.  
585 W., et al. (2021). Brine-driven destruction of clay minerals in Gale crater, Mars.  
586 *Science*, 373(6551), 198-204. <https://doi.org/10.1126/science.abg5449>

587 Carter, J., Loizeau, D., Mangold, N., Poulet, F., & Bibring, J. (2015). Widespread  
588 surface weathering on early Mars: A case for a warmer and wetter climate. *Icarus*,  
589 248, 373-382. <https://doi.org/10.1016/j.icarus.2014.11.011>

590 Carter, J., Poulet, F., Bibring, J. P., Mangold, N., & Murchie, S. (2013). Hydrous  
591 minerals on Mars as seen by the CRISM and OMEGA imaging spectrometers:  
592 Updated global view: Hydrous minerals on Mars: Global view. *Journal of*  
593 *Geophysical Research: Planets*, 118(4), 831-858.  
594 <https://doi.org/10.1029/2012JE004145>

595 Chauviré B., Pineau, M., Quirico, E., & Beck, P. (2021). Near infrared signature of  
596 opaline silica at Mars-relevant pressure and temperature. *Earth and Planetary*  
597 *Science Letters*, 576(15), 117239. <https://doi.org/10.1016/j.epsl.2021.117239>

598 Cuadros, J. (1997). Interlayer cation effects on the hydration state of smectite. *American*  
599 *Journal of Science*, 297, 829-841. <https://doi.org/10.2475/ajs.297.8.829>

600 Cuadros, J., Mavris, C., Michalski, J. R., Nieto, J. M., Bishop, J. L., & Fiore, S. (2019).  
601 Abundance and composition of kaolinite on Mars: Information from NIR spectra  
602 of rocks from acid-alteration environments, Riotinto, SE Spain. *Icarus*, 330(15),  
603 30-41. <https://doi.org/10.1016/j.icarus.2019.04.027>

604 Cuadros, J., & Michalski, J. R. (2013). Investigation of Al-rich clays on Mars: Evidence  
605 for kaolinite–smectite mixed-layer versus mixture of end-member phases. *Icarus*,  
606 222(1), 296-306. <https://doi.org/10.1016/j.icarus.2012.11.006>

607 Cuadros, J., Michalski, J. R., Dekov, V., & Bishop, J. L. (2016). Octahedral chemistry  
608 of 2:1 clay minerals and hydroxyl band position in the near-infrared: Application

609 to Mars. *American Mineralogist*, 101(3), 554-563. <https://doi.org/10.2138/am->  
610 [2016-5366](https://doi.org/10.2138/am-2016-5366)

611 Ding, Z., & Frost, R. L. (2002). Controlled rate thermal analysis of nontronite.  
612 *Thermochimica Acta*, 389(1-2), 185-193. [https://doi.org/10.1016/](https://doi.org/10.1016/S0040-) [S0040-](https://doi.org/10.1016/S0040-6031(02)0059-X)  
613 [6031\(02\)0059-X](https://doi.org/10.1016/S0040-6031(02)0059-X)

614 Ehlmann, B. L., Berger, G., Mangold, N., Michalski, J. R., Catling, D. C., Ruff, S. W.,  
615 et al. (2013). Geochemical consequences of widespread clay mineral formation in  
616 Mars' ancient crust. *Space Science Reviews*, 174(1 - 4), 329–364.  
617 <https://doi.org/10.1007/s11214-012-9930-0>

618 Ehlmann, B. L., Mustard, J. F., Clark, R. N., Swayze, G. A., & Murchie, S. L. (2011a).  
619 Evidence for low-grade metamorphism, hydrothermal alteration, and diagenesis  
620 on Mars from phyllosilicate mineral assemblages. *Clays and Clay Minerals*, 59(4),  
621 359-377. <https://doi.org/10.1346/ccmn.2011.0590402>

622 Ehlmann, B. L., Mustard, J. F., Murchie, S. L., Bibring, J. P., Meunier, A., Fraeman, A.  
623 A., & Langevin, Y. (2011b). Subsurface water and clay mineral formation during  
624 the early history of Mars. *Nature*, 479(7371), 53-60.  
625 <https://doi.org/10.1038/nature10582>

626 Ehlmann, B. L., Mustard, J. F., Swayze, G. A., Clark, R. N., Bishop, J. L., Poulet, F., et  
627 al. (2009). Identification of hydrated silicate minerals on Mars using MRO-  
628 CRISM: Geologic context near Nili Fossae and implications for aqueous alteration.  
629 *Journal of Geophysical Research*, 114(E2), E00D08.  
630 <https://doi.org/10.1029/2009JE003339>

631 Fernandez-Caliani, J. C., Crespo, E., Rodas, M., Barrenechea, J. F., & Luque, F. J.  
632 (2004). Formation of nontronite from oxidative dissolution of pyrite disseminated  
633 in precambrian felsic metavolcanics of the Southern Iberian Massif (Spain). *Clays  
634 and Clay Minerals*, 52, 106-114. <https://doi.org/10.1346/CCMN.2004.0520110>

635 Fox, V. K., Kupper, R. J., Ehlmann, B. L., Catalano, J. G., Razzell-Hollis, J., Abbey, W.  
636 J., et al. (2021). Synthesis and characterization of Fe(III)-Fe(II)-Mg-Al smectite  
637 solid solutions and implications for planetary science. *American Mineralogist*,  
638 106(6), 964-982. <https://doi.org/10.2138/am-2020-7419CCBYNCND>

639 Frost, R. L., Klopogge, J. T., & Ding, Z. (2002). The Garfield and Uley nontronites -  
640 an infrared spectroscopic comparison. *Spectrochimica Acta Part A-Molecular and  
641 Biomolecular Spectroscopy*, 58, 1881-1894. [https://doi.org/10.1016/S1386-  
642 1425\(01\)00638-2](https://doi.org/10.1016/S1386-1425(01)00638-2)

643 Gainey, S. R., Hausrath, E. M., Hurowitz, J. A., & Milliken, R. E. (2014). Nontronite  
644 dissolution rates and implications for Mars. *Geochimica et Cosmochimica Acta*,  
645 126, 192-211. <https://doi.org/10.1016/j.gca.2013.10.055>

646 Gaudin, A., Dehouck, E., & Mangold, N. (2011). Evidence for weathering on early  
647 Mars from a comparison with terrestrial weathering profiles. *Icarus*, 216(1), 257-  
648 268. <https://doi.org/10.1016/j.icarus.2011.09.004>

649 He, H., Ji, S., Tao, Q., Zhu, J., Chen, T., Liang, X., et al. (2017). Transformation of  
650 halloysite and kaolinite into beidellite under hydrothermal condition. *American  
651 Mineralogist*, 102(5), 997-1005. <https://doi.org/10.2138/am-2017-5935>

652 Hunt, G. R. (1977). Spectral signatures of particulate minerals in the visible and near

653 infrared. *Geophysics*, 42(3), 501-513. <https://doi.org/10.1190/1.1440721>

654 Hunt, G. R., & Ashley, R. P. (1979). Spectra of altered rocks in the visible and near  
655 infrared. *Economic Geology*, 74(7), 1613-1629.  
656 <https://doi.org/10.2113/gsecongeo.74.7.1613>

657 Kawi, S., & Yao, Y. Z. (1999). Saponite catalysts with systematically varied Mg/Ni  
658 ratio: Synthesis, characterization, and catalysis. *Microporous & Mesoporous  
659 Materials*, 33(1-3), 49-59. [https://doi.org/10.1016/S1387-1811\(99\)00122-5](https://doi.org/10.1016/S1387-1811(99)00122-5)

660 Li, S., He, H., Tao, Q., Zhu, J., Tan, W., Ji, S., et al. (2020). Kaolinization of 2:1 type  
661 clay minerals with different swelling properties. *American Mineralogist*, 105(5),  
662 687-696. <https://doi.org/10.2138/am-2020-7339>

663 Liu, J., He, H., Michalski, J., Cuadros, J., Yao, Y., Tan, W., et al. (2021a). Reflectance  
664 spectroscopy applied to clay mineralogy and alteration intensity of a thick basaltic  
665 weathering sequence in Hainan Island, South China. *Applied Clay Science*, 201,  
666 105923. <https://doi.org/10.1016/j.clay.2020.105923>

667 Liu, J., Michalski, J., Tan, W., He, H., & Xiao, L. (2021b). Anoxic chemical weathering  
668 under a reducing greenhouse on early Mars. *Nature Astronomy*, 5, 503–509.  
669 <https://doi.org/10.1038/s41550-021-01303-5>

670 Lowe, D. R., Bishop, J. L., Loizeau, D., Wray, J. J., & Beyer, R. A. (2020). Deposition  
671 of >3.7 Ga clay-rich strata of the Mawrth Vallis Group, Mars, in lacustrine, alluvial,  
672 and aeolian environments. *Geological Society of America Bulletin*, 132(1-2), 17-  
673 30. <https://doi.org/10.1130/B35185.1>

674 Madejov  J., Janek, M., Komadel, P., Herbert, H. J., & Moog, H. C. (2002). FTIR

675 analyses of water in MX-80 bentonite compacted from high salinity salt solution  
676 systems. *Applied Clay Science*, 20(6), 255-271. <https://doi.org/10.1016/S0169->  
677 [1317\(01\)00067-9](https://doi.org/10.1016/S0169-1317(01)00067-9)

678 Madejov  J., & Komadel, P. (2001). Baseline studies of the clay minerals society  
679 source clays: infrared methods. *Clay and Clay Minerals*, 49, 410-432.  
680 <https://doi.org/10.1346/CCMN.2001.0490508>

681 Mart nez-Alonso, S., Rustad, J. R., & Goetz, A. F. H. (2002). Ab initio quantum  
682 mechanical modeling of infrared vibrational frequencies of the OH group in  
683 dioctahedral phyllosilicates. Part II: Main physical factors governing the OH  
684 vibrations. *American Mineralogist*, 87(8-9), 1224-1234.  
685 <https://doi.org/10.2138/am-2002-8-922>

686 McKeown, N. K., Bishop, J. L., Noe Dobrea, E. Z., Ehlmann, B. L., Parente, M.,  
687 Mustard, J. F., et al. (2009). Characterization of phyllosilicates observed in the  
688 central Mawrth Vallis region, Mars, their potential formational processes, and  
689 implications for past climate. *Journal of Geophysical Research*, 114(E2).  
690 <https://doi.org/10.1029/2008JE003301>

691 Michalski, J. R., Bibring, J. P., Poulet, F., Loizeau, D., Mangold, N., Dobrea, E.N., et  
692 al. (2010). The Mawrth Vallis Region of Mars: A Potential Landing Site for the  
693 Mars Science Laboratory (MSL) Mission. *Astrobiology*, 10, 687-703.  
694 <https://doi.org/10.1089/ast.2010.0491>

695 Michalski, J. R., Cuadros, J., Bishop, J. L., Darby Dyar, M., Dekov, V., & Fiore, S.  
696 (2015). Constraints on the crystal-chemistry of Fe/Mg-rich smectitic clays on

697 Mars and links to global alteration trends. *Earth and Planetary Science Letters*,  
698 427, 215-225. <https://doi.org/10.1016/j.epsl.2015.06.020>

699 Michalski, J. R., Niles, P. B., Cuadros, J., & Baldrige, A. M. (2013). Multiple working  
700 hypotheses for the formation of compositional stratigraphy on Mars: Insights from  
701 the Mawrth Vallis region. *Icarus*, 226, 816-840.  
702 <https://doi.org/10.1016/j.icarus.2013.05.024>

703 Michalski, J. R., & Noe Dobrea, E. Z. (2007). Evidence for a sedimentary origin of clay  
704 minerals in the Mawrth Vallis region, Mars. *Geology*, 35, 951-954.  
705 <https://doi.org/10.1130/g23854a.1>

706 Nahon, D., Colin, F., & Tardy, Y. (1982). Formation and distribution of Mg, Fe, Mn-  
707 smectites in the first stages of the lateritic weathering of forsterite and tephroite.  
708 *Clay Minerals*, 17(3), 339-348. <https://doi.org/10.1180/claymin.1982.017.3.06>

709 Pineau, M., Mathian, M., Baron, F., Rondeau, B., Le Deit, L., Allard, T., & Mangold,  
710 N. (2022). Estimating kaolinite crystallinity using near-infrared spectroscopy:  
711 Implications for its geology on Earth and Mars. *American Mineralogist*, 107(8),  
712 1453-1469. <https://doi.org/10.2138/am-2022-8025>

713 Prudencio, M. I., Braga, M. A. S., Paquet, H., Waerenborgh, J. C., Pereira, L. C. J., &  
714 Gouveia, M. A. (2002). Clay mineral assemblages in weathered basalt profiles  
715 from central and southern Portugal: climatic significance. *Catena*, 49, 77-89.  
716 [https://doi.org/10.1016/S0341-8162\(02\)00018-8](https://doi.org/10.1016/S0341-8162(02)00018-8)

717 Rivera Banuchi, V. B., Liu, W., Yee, N., Legett, C., Glotch, T. D., & Chemtob, S. M.  
718 (2022). Ultraviolet photooxidation of Smectite - bound Fe(II) and implications for

719 the origin of Martian nontronites. *Journal of Geophysical Research: Planets*, 127,  
720 e2021JE007150. <https://doi.org/10.1029/2021JE007150>

721 Tan, W., Qin, X., Liu, J., Zhou, M., He, H., Yan Wang, C., et al. (2022). Feasibility of  
722 visible short-wave infrared reflectance spectroscopy to characterize regolith-  
723 hosted rare earth element mineralization. *Economic Geology*, 117(2), 495-508.  
724 <https://doi.org/10.5382/econgeo.4877>

725 Viviano-Beck, C. E., Seelos, F. P., Murchie, S. L., Kahn, E. G., Seelos, K. D., Taylor,  
726 H. W., et al. (2014). Revised CRISM spectral parameters and summary products  
727 based on the currently detected mineral diversity on Mars. *Journal of Geophysical*  
728 *Research: Planets*, 119(6), 1403-1431. <https://doi.org/10.1002/2014JE004627>

729 Viviano, C. E., Moersch, J. E., & McSween, H. Y. (2013). Implications for early  
730 hydrothermal environments on Mars through the spectral evidence for carbonation  
731 and chloritization reactions in the Nili Fossae region. *Journal of Geophysical*  
732 *Research: Planets*, 118(9), 1858-1872. <https://doi.org/10.1002/jgre.20141>

733 Wilson, M. J. (2004). Weathering of the primary rock-forming minerals: processes,  
734 products and rates. *Clay Minerals*, 39(3), 233-266.  
735 <https://doi.org/10.1180/0009855043930133>

736 Wray, J. J., Ehlmann, B. L., Squyres, S. W., Mustard, J. F., & Kirk, R. L. (2008).  
737 Compositional stratigraphy of clay-bearing layered deposits at Mawrth Vallis,  
738 Mars. *Geophysical Research Letters*, 35(12).  
739 <https://doi.org/10.1029/2008GL034385>

740 Wray, J. J., Murchie, S. L., Squyres, S. W., Seelos, F. P., & Tornabene, L. L. (2009).

741       Diverse aqueous environments on ancient Mars revealed in the southern highlands.  
742       *Geology*, 37(11), 1043-1046. <https://doi.org/10.1130/g30331a.1>

743   Ye, B., & Michalski, J. R. (2021). Precipitation - Driven Pedogenic Weathering of  
744       Volcaniclastics on Early Mars. *Geophysical Research Letters*, 48(5), 1–10.  
745       <https://doi.org/10.1029/2020GL091551>

746   Zhang, C., He, H., Tao, Q., Ji, S., Li, S., Ma, L., et al. (2017). Metal occupancy and its  
747       influence on thermal stability of synthetic saponites. *Applied Clay Science*, 135,  
748       282-288. <https://doi.org/10.1016/j.clay.2016.10.006>

749   Zhang, L., Fu, X., Wang, A., & Ling, Z. (2022). Crystallinity effects on the vibrational  
750       spectral features of saponite: Implications for characterizing variable crystalline  
751       phyllosilicates on Mars. *Icarus* 379, 114951.  
752       <https://doi.org/10.1016/j.icarus.2022.114951>